Chemo-mechanical Instability of Light-induced Humidity Responsive Bilayered Actuators

Wenrui Ma, Kin Wa Kwan*, Runni Wu, Alfonso H.W. Ngan
Department of Mechanical Engineering, The University of Hong Kong, HKSAR

*Corresponding author. E-mail: kkwkwan@connect.hku.hk
Postal address: 7F Haking Wong Building, Department of Mechanical Engineering, The University of Hong Kong, Pokfulam Road, HKSAR

Abstract:

Recently discovered light-induced bilayered actuators comprising a light-responsive actuating layer supported by a passive layer are versatile in miniaturized robotics applications, owing to their simple, compact construction and wireless, self-contained mode of actuation. However, the chemo-mechanics and quantitative description of their actuation mechanisms are not sufficiently understood. Here, based on a chemo-mechanics model, a novel instability phenomenon leading to extraordinarily large magnitudes of the bending actuation of bilayered actuators is found and experimentally proven. At specific ratios of the elastic moduli and thicknesses of the active and passive layers, and activation volume of the actuation mechanism, the actuation of the active layer will be put into a positive feedback mode where the actuation-induced bending of the cantilever structure triggers a compressive stress in a surface region of the active layer which enhances further contractive actuation of the latter by means of light-induced water de-intercalation. The beneficial instability is observed and analysed for two active material systems that exhibit such a light-induced water de-intercalation mechanism, namely, cobalt-oxides/hydroxides (C-O-H) and nickel hydroxide/oxyhydroxide (N-H-O). Experimental results agree well with predictions of the chemo-mechanics model, thus verifying its applicability to design high-performing actuation systems.

Keywords: bilayered actuator, instability, cobalt oxides/hydroxides, light-induced actuation

1. Introduction

Bilayered actuators consisting of an actuating layer supported by a passive layer are a common form of artificial muscles for powering microrobotics and miniaturized devices [1–5]. The active, actuating layer is composed of at least one material that contracts or expands under an applied stimulus, and although the intrinsic strains of many actuating materials are less than 1% [5–9], the constraining effect of the passive layer often leads to large bending or curling of the bilayer. As a bilayered actuator is thin and compact with a simple structure and the actuation is self-contained without requiring other components to function, it can be applied to confined environments where conventional electromechanical movers are too bulky to be used. To date, bilayered actuators that respond to applied voltage [10,11], electrochemical potential [6,7,12], heat [13–16], light illumination [5,17–19], humidity change [5,13,20,21] and other stimuli [22,23], have been developed, showing the possibilities to be applied in different contexts.

Due to the abovementioned advantages, bilayered actuator is a topic that has continuously attracted a great deal of attention [21,24]. Although mismatch strains of bilayers have been studied thoroughly as a classical mechanics topic [25–27], few efforts have addressed the interplay between the mechanics of the bilayer and the physio-chemical mechanism of the actuation of the active layer. Based on the classical Timoshenko beam theory [27], we recently developed a model to describe the chemo-mechanics of the light-induced actuation of cobalt-oxides/hydroxides (C-O-H) bilayered actuator [28] . In this paper, we apply this model to analyse the experimental results from both C-O-H and nickel hydroxide/oxyhydroxide (N-H-O), on both nickel and polycarbonate substrates with a large range of the ratio ($\alpha := h_a/h_s$) between the thickness of the actuating layer (h_a) and the supporting layer (h_s). Both C-O-H and N-H-O are recently discovered light/humidity-responsive actuating materials that exhibit shrinkage on visible-light illumination [5,28], and the choice of the nickel and polycarbonate substrates allows the ratio ($\beta := E_a/E_s$) between the

Young modulus of the actuating layer (E_a) and the supporting layer (E_s) to vary in a wide range. To our surprise, we observed a chemo-mechanical instability phenomenon that has not been reported before: the actuation surges to a large magnitude in a narrow range of α, thus enabling ultra-high actuation performance to be realized. This paper also shows that the chemo-mechanics model can provide a quantitative understanding of bilayered actuators, and, in particular, can predict the performance of such actuators made of different materials and configurational parameters, for design of engineering devices.

2. Methods

2.1 Experimental – fabrication and actuation characterization of actuators

Chemicals and Materials: Chemicals for the electrodeposition of active layers were purchased from Sigma-Aldrich without further purification: nickel sulfate heptahydrate ($NiSO_4{\cdot}7H_2O$), cobalt sulfate heptahydrate ($CoSO_4{\cdot}7H_2O$) ReagentPlus® ≥99%, sodium acetate (CH_3COONa) and sodium sulfate (Na_2SO_4) in puriss. p.a., anhydrous ≥98%. The solution bath of C-O-H contains $CoSO_4{\cdot}7H_2O$, CH_3COONa, and Na_2SO_4, all at 0.05 M, and that of nickel hydroxide/oxyhydroxide (N-H-O) contains 0.13 M $NiSO_4{\cdot}7H_2O$, 0.13 M CH_3COONa, and 0.1 M Na_2SO_4. Deionized (DI) water with a resistivity of ~18 MΩ·cm was used to make the solution baths and for rinsing. The solution bath for electrodepositing Ni substrates was purchased from Caswell, Inc., and that for the Au layer contains 1.7 M Na_2SO_3 and Au plating solution (Oromerse SO Part B, Technic) in the volume ratio 9:1.

Micro-porous polycarbonate (MPPC) substrates: Nuclepore Track-Etched polycarbonate membranes (Whatman®) with a diameter of 25 mm and a pore size of 1 μm were used as one type of substrates. Such membranes are coated with a layer of poly(vinylpyrrolidone) (PVP) during production to make them hydrophilic [29,30], and their thickness was measured to be

10 μm by a profilometer (DektakXT, Bruker). Prior to the active-layer electrodeposition, the membranes were metallized by sputtering a 14-nm thick Au layer using a Bal-tec SCD 005 Sputter Coater (working distance: 50 mm, sputtering current: 30 mA, sputtering duration: 100 s). Then, they were adhered to glass slides by applying a tiny amount of lacquer on the edge, so that the vigorous stirring during the electrodeposition will not crumple the membranes. The active material of either C-O-H or N-H-O was anodically electrodeposited on the substrate in a three-electrode cell at the same current density of 0.545 mA/cm^2 against saturated calomel reference electrode (SCE) and Pt mesh counter electrode under vigorous stirring. Different thickness (h_a) was achieved by varying the duration of electrodeposition. As the Au layer is very thin and inactive, the deposited films with MPPC substrates are therefore effectively bilayered cantilevers. Lastly, the lacquer was gently scraped off and the freed off bilayered films were cut into longitudinal strips of 20 mm by 2.5 mm which were fixed at one end for actuation tests.

Nickel substrates: Nickel films were also used as another type of substrates. First, Ni was cathodically electrodeposited on fluorine-doped tin oxide (FTO)-coated glass slides (Sigma-Aldrich, ~10 ohms/square) masked by a chemical-resist sticker (CM-200E, Max Bepop) with rectangular openings (the typical size was 22 mm by 2 mm). A constant cathodic current density of −15 mA/cm^2 was applied for 5 min on the FTO immersed in the Ni bath in a two-electrode electrochemical cell against a Ni metal sheet counter electrode. To improve the adhesion of the active layer on Ni, a thin Au layer was electrodeposited on the Ni in the Au bath with −0.1 mA/cm^2 applied to the Ni-plated FTO in a two-electrode cell against a platinum (Pt) mesh counter electrode for 30 min. Lastly, N-H-O or C-O-H was anodically electrodeposited on the substrates in a three-electrode cell at 0.545 mA/cm^2 against saturated calomel reference electrode (SCE) and Pt mesh counter electrode under vigorous stirring.

Different thickness (h_a) was achieved by varying the duration of electrodeposition. Lastly, the actuators were peeled off from the FTO by a pair of sharp tweezers and adhered to a piece of Cu tape (3M) for the actuation tests. The size was then reduced to about 20 mm by 2 mm.

Light-induced actuation tests: Actuation tests were performed inside a semi-closed compartment. The actuation was induced by visible light from a Xenon light source (GLORIA-X500A, Zolix). Actuators with different active and substrate materials and different thickness ratios were fabricated and tested under Vis light intensities of 10, 20 and 50 mW/cm^2. The illumination time was prolonged and illuminating direction was tuned (see Supplementary Video S1) to enable the actuation to reach steady state, and the actuation process was recorded by a digital camera (Panasonic Lumix DMC-LX10). Curvature changes κ were then measured from the initial and final states of the actuators in the videos by best-fitting their shapes with circles, i.e. for a bent actuator, the curvature was measured as $\kappa = 2/d$, where d is the diameter of the best-fitting circle. For actuators that curled into more than 1 loop, $\kappa = 2n\pi/(L - L_0)$ is used, where n is the number of curling loops, L is the length of the actuator and L_0 is the length of inactive part of the actuator due to geometric inaccessibility of light or other reasons.

Photothermal measurements: C-O-H was anodically electrodeposited on MPPC and Ni substrates using the fabrication conditions above. The actuators were then cut into strips and adhered to transparent plastic sheets by double-sided tapes and placed at the center of a light spot from the light source. The distance between the light source and the actuator was controlled to give light intensities of either 20 or 50 mW/cm^2 at the actuator. Temperature changes of the actuators and the adjacent regions were recorded throughout the illumination and cooling processes by an IR thermal camera (FLIR SC7700BB) for analysis.

2.2 Theory

2.2.1 Chemo-mechanics model

Under stimuli such as light illumination or a reduction in the environmental humidity, the present C-O-H and N-H-O active materials contract, presumably due to the de-intercalation of water molecules from their "turbostratic" crystal structure [5]. Therefore, when C-O-H or N-H-O is used in the active layer of a bilayer structure, the stimulation will cause the bilayer to bend as shown in Fig. 1a. However, for a thicker active layer, the bending actuation has also a diffusive component [28]: the light stimulation or environmental humidity first sets the top surface region of the active layer into a state of reduced water concentration and hence actuation strain ε_a^{chem}. Then, a concentration gradient of water is set up across the thickness of the active layer, causing water in the subsurface parts of the active layer to diffuse to the surface (where the concentration is maintained at a low level by the stimuli), and the cantilever to bend gradually. This process is schematically illustrated in (Fig. 1b) and is analysed in detail in Kwan and Ngan [28]. Eventually, when the subsurface water concentration drops to the surface value, the diffusion stops, the bending actuation is completed, and the entire active layer will have the same actuation strain ε_a^{chem} as that of the surface maintained by the stimuli. At the final state where diffusion and hence bending are completed, although the actuation strain is uniform at the value ε_a^{chem} across the active layer's thickness, the stress has a gradient since cantilever is bent; we let σ_a to be the stress at the stimulated surface, $\bar{\sigma}_a$ to be the average stress in the active layer, and $\sigma_a \neq \bar{\sigma}_a$ due to the bending.

Chemical characteristics – In the present stimuli-responsive actuating materials such as C-O-H, the light or environmental humidity stimuli triggers a shift in the equilibrium between the water de-intercalated (smaller in volume) and water intercalated (larger in volume) states:

C-O-H (water de-intercalated, smaller in volume) ⇌ C-O-H (water intercalated, larger in volume),

with a reaction constant K_{eq} given by:

$$(1 + 3\varepsilon_a^{chem}) \approx K_{eq} = \frac{[\text{C–O–H (larger)}]}{[\text{C–O–H (smaller)}]} = \exp\left(-\frac{\Delta E_{chem} - \sigma_a \Omega}{k_B T}\right)$$

Here, [C-O-H (larger)] and [C-O-H (smaller)] are the concentrations of the water intercalated and de-intercalated states, respectively, of the active material C-O-H, and so their ratio K_{eq} minus unity is the volumetric strain $3\varepsilon_a^{chem}$, the zero-point of which is taken to be when $K_{eq} = 1$. The second part of the above equation represents the hypothesis that water de-intercalation from the C-O-H structure is a thermally activated process enhanced by a compressive stress, where ΔE_{chem} is the chemical driving force for water de-intercalation granted by the light stimulation, σ_a (positive if tensile) is the actuation stress provided by the active material, Ω is the activation volume, and k_B is Boltzmann's constant [28]. The above equation can be re-arranged to give:

$$\sigma_a \Omega = \Delta E_{chem} + k_B T \ln(1 + 3\varepsilon_a^{chem}) \approx \Delta E_{chem} + 3 k_B T \varepsilon_a^{chem} \quad (1)$$

Once again, it is important to note that the stress σ_a in Eq. (1) is that at the top, stimulated surface of the active layer.

Mechanics characteristics – As mentioned above, at the *completed* state of the actuation where diffusion has stopped, the entire active layer will exhibit the same actuation strain ε_a^{chem} maintained by the stimuli at the surface as given by Eq. (1), but the average stress $\bar{\sigma}_a$ in the active layer is not the same as the surface stress σ_a in Eq. (1) since the active layer is bent. According to Timoshenko's classical theory for mismatch-strain bending [27,28], $\bar{\sigma}_a$ is given by force (*P*) and moment (*M*) equilibrium (Fig. 1b) as:

$$\bar{\sigma}_a = \frac{P}{h_a} = \frac{1}{\bar{B}_a} \kappa, \quad (2)$$

where

$$\bar{B}_a = \frac{6h_a(h_a+h_s)}{E_a h_a^3+E_s h_s^3}$$

and the mismatch strain between the two layers is given as

$$\varepsilon_a^{chem} = -\bar{C}_a \bar{\sigma}_a \tag{3}$$

where

$$\bar{C}_a = \frac{1}{E_a} + \frac{h_a}{E_s h_s} + \frac{3h_a(h_a+h_s)^2}{E_a h_a^3+E_s h_s^3} \tag{4}$$

In the above, E_a and E_s are the elastic moduli of the active layer and substrate respectively, and h_a and h_s are their thicknesses. The mismatch strain ε_a^{chem} represents the strain that would be measured from the active layer under stimulation if it were detached from the substrate, and in Timoshenko's theory for thermal mismatch [27], this is simply the difference in thermal expansion coefficients of the two layers, multiplied by the temperature increase.

Whereas Timoshenko's Eqs. (2-4) cast the problem in terms of the *average* actuation stress $\bar{\sigma}_a$ in the active layer, to relate to the chemical characteristics in Eq. (1) in which the surface stress σ_a is involved, we note the following relation between the two:

$$\sigma_a = \bar{\sigma}_a - \frac{E_a\, h_a}{2}\, \kappa = D_a \kappa \tag{5}$$

where

$$D_a = \frac{E_a h_a^3+E_s h_s^3}{6h_a(h_a+h_s)} - \frac{E_a\, h_a}{2}$$

From Eqs. (2), (3) and (5), we therefore have

$$\varepsilon_a^{chem} = -C_a \sigma_a \tag{6}$$

where

$$C_a = \left[\frac{(h_a+h_s)}{2} + \frac{E_a h_a^3+E_s h_s^3}{6(h_a+h_s)}\left(\frac{1}{E_a h_a} + \frac{1}{E_s h_s}\right)\right] / \left[\frac{E_a h_a^3+E_s h_s^3}{6h_a(h_a+h_s)} - \frac{E_a\, h_a}{2}\right] \tag{7}$$

Chemo-mechanics equilibrium – At equilibrium, Eqs. (1) and (6) are to be satisfied simultaneously, leading to a solution for $(\sigma_a, \varepsilon_a^{chem})$. Substituting the solution for σ_a into Eq. (5) yields the actuation curvature κ expressed in a normalized form as:

$$K \coloneqq \frac{\kappa h_s}{\phi \beta^{1/3}} = \frac{6\alpha\beta^{2/3}(1+\alpha)}{(1+\alpha\beta)(1+\alpha^3\beta)+\omega[1-\alpha^2\beta(3+2\alpha)]+3\alpha\beta(1+\alpha)^2} \tag{8}$$

where $\alpha = h_a/h_s$, $\beta = E_a/E_s$, $\phi = \Delta E_{chem}/(3k_BT)$ and $\omega = E_a\Omega/(3k_BT)$. K above is a normalized measure of the curvature performance, since a higher K means that (i) the active material can bend a substrate with a higher bending stiffness $E_s h_s^3$ to the same curvature κ, or substrates of the same bending stiffness $E_s h_s^3$ to a higher curvature κ, and (ii) a lower driving force ϕ is needed for the same curvature and substrate bending stiffness.

The parameters ϕ and ω are normalized measures for the thermodynamic driving force ΔE_{chem}, and the activation volume Ω, respectively, and hence they are figures of merit of the actuating material. In particular, ϕ directly indicates the magnitude of the thermodynamic driving force for the actuation provided by the stimulation, and hence it is a more important figure of merit. The chemo characteristics of the actuation in Eq. (1) can also be recast in these two parameters as:

$$\varepsilon_a^{chem} = \left(\frac{\sigma_a}{E_a}\right)\omega - \phi \tag{9}$$

From Eq. (9), it can be seen that the normalized driving force ϕ is also the stress-free actuation strain, i.e. $\phi = -\varepsilon_a^{chem}(\sigma_a = 0)$. Plotting ε_a^{chem} against σ_a/E_a would yield ω as the slope and ϕ as the minus of the y-intercept.

2.2.2 Chemo-mechanical instability

For sufficiently large actuation of the bilayer cantilever, σ_a can become negative, as the bending of the bilayer turns the top surface region of the active layer into a compressive stress state, even though the intrinsic actuation strain ε_a^{chem} of the stimulated material there which

drives the actuation is contractive (negative), and the average actuation stress $\bar{\sigma}_a$ in the entire active layer (c.f. Eq. (3)) is tensile (positive). Then, according to the chemical characteristics in Eq. (1), a compressive (negative) stress σ_a in the actuating material will further enhance the actuation, i.e. make ε_a^{chem} more contractive (negative), and this in turn will further increase the bending of the bilayer, making σ_a at the top surface region even more compressive. The interplay between the chemical kinetics and mechanics of the bilayer therefore results in a positive feedback scenario in which the actuation increases in an unstable manner.

Mathematically, the phenomenon of a contractive actuation ε_a^{chem} leading to a compressive surface stress σ_a via bending of the bilayer is associated with a negative C_a in Eq. (6). As shown in Fig. 1c, as C_a becomes increasingly negative, the magnitude of the equilibrium ε_a^{chem} will increase, and when C_a is sufficiently negative, the mechanics characteristics (Eq. (6), orange solid line) can have the same slope as the chemical characteristics (Eq. (1), green line), resulting in an instability condition where $\varepsilon_a^{chem} \to -\infty$. This instability arises theoretically as

$$E_a C_a = -\omega \tag{10}$$

when the two characteristics in Eqs. (1) and (6) adopt the same slope. From Eq. (7), $E_a C_a$ can be written in a normalized form as:

$$E_a C_a = \frac{3\alpha\beta(1+\alpha)^2+(1+\alpha\beta)(1+\alpha^3\beta)}{1-\alpha^2\beta(2\alpha+3)}, \tag{11}$$

and Fig. 1d shows that the plot of $E_a C_a(\alpha, \beta)$ exhibits two branches separated by the curve $\beta = 1/\alpha^2(2\alpha + 3)$ along which the denominator in Eq. (11) vanishes, and across which $E_a C_a$ changes from +∞ to -∞. For the inner branch $\beta < 1/\alpha^2(2\alpha + 3)$, $E_a C_a(\alpha, \beta)$ varies from 1 to ∞, and for the outer branch $\beta > 1/\alpha^2(2\alpha + 3)$, $E_a C_a(\alpha, \beta)$ varies from -∞ to -2; in other words, $E_a C_a$ adopts no value between -2 and 1 in the domain $\alpha, \beta > 0$ (see Appendix for

details). This means that the instability condition in Eq. (10) can happen only for $\omega > 2$. Note that the instability is a merit, as it gives a large actuation, as mentioned above.

Examples of a stable case ($\omega = 0.55$, smaller than the threshold of 2) and an unstable case ($\omega = 5.9$, larger than the threshold of 2) are shown in Fig. 1(e, f), respectively. For the stable case when ω is small, $K(\alpha, \beta)$ shows a mild hump in the domain $0 < \alpha < 2$, $0 < \beta < 1$, with a peak value of about 1.2. However, for the unstable case when ω is large, K exhibits a low value with a slowly varying trend when α, β are small, but a sudden increase to infinity takes place when the curve $\beta = 1/\alpha^2(2\alpha + 3)$ is approached, across which K exhibits a singularity behavior. Thus, we define the (α, β) domain in vicinity of the curve $\beta = 1/\alpha^2(2\alpha + 3)$ as the instability region.

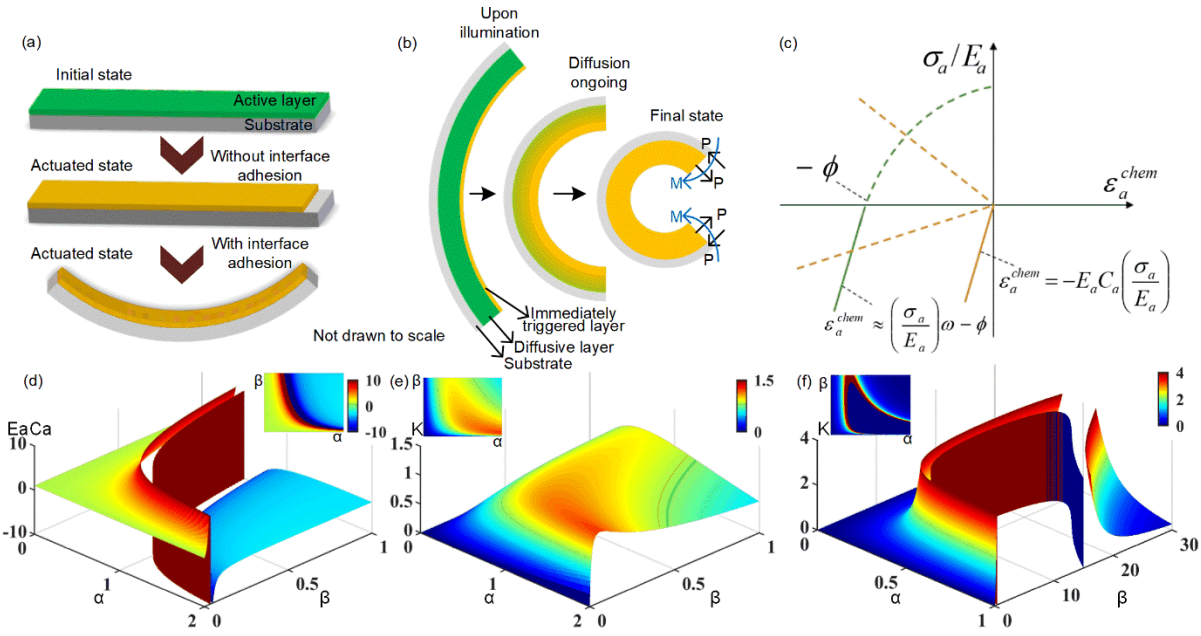

Fig. 1 (a) Schematic of actuating response of a bilayered cantilever comprising an active layer on top supported by a passive substrate layer. (b) Diffusion model of cantilever actuator. (c) Chemo-mechanics equilibrium and instability. When C_a becomes negative, the equilibrium actuation strain increases in magnitude, and when C_a is sufficiently negative, the mechanics characteristics (orange solid line) would not meet the chemo-characteristics (green line),

resulting in an instability condition where the actuation strain becomes infinitely large. (d) Surface and contour plots of $E_a C_a(\alpha, \beta)$. (e,f) $K(\alpha, \beta)$ plots for chemo-mechanically (e) stable case ($\omega = 0.55$) and (f) unstable case ($\omega = 5.9$).

3. Results and Analysis

3.1 Quantitative characterization of C-O-H actuators

Detailed materials characterization and the actuation mechanism of the light-responsive material C-O-H can be found in our previous work. Briefly, volume change of C-O-H is caused by light-induced water de-intercalation from the turbostratic crystal structure, and in the bilayer configuration the mismatch in the lengths of the active layer and substrate therefore results in the bending or curling motion of the actuator. Fig. 2a shows the typical SEM micrograph of a bilayer actuator, with a C-O-H active layer deposited on top of an MPPC substrate layer. The actuation response of a typical C-O-H/MPPC actuator under 50mW/cm^2 Vis light illumination is shown in Fig. 2b. With the C-O-H layer on the right and MPPC on the left, the actuator curled slightly leftward initially, and then under light illumination it curled into a number of loops. The curvature changes κ between the actuated and initial states at various intensities for different h_a were measured, and $\bar{\sigma}_a$ and ε_a^{chem} were calculated by Eqs. (2) and (3) for quantitative analysis, with E_a and E_s meausred as 17 GPa and 0.7 GPa respectively and h_s as 10 μm.

As shown in Fig. 2c, three different Vis light intensities (10, 20 and 50mW/cm^2) were used for analysis and an overall higher κ was observed at higher illuminating light intensity, and a mild increasing trend with α with intensifying fluctuation can also be seen. Such a fluctuation arises from the above-mentioned chemo-mechanical instability, which will be explained in section 3.2. The plot of $\bar{\sigma}_a$ against α in Fig. 2d shows a similar trend, as $\bar{B}_a = \frac{6h_a(h_a+h_s)}{E_a h_a^3+E_s h_s^3}$ in Eq. (2) varies within a narrow range for the α values studied as shown in the inset of Fig. 2d. However, ε_a^{chem} shows a steeper rising trend against α as shown in Fig. 2e, as $-\varepsilon_a^{chem} = \bar{C}_a\bar{\sigma}_a$ (Eq. (3)) and $\bar{C}_a = \frac{1}{E_a} + \frac{h_a}{E_s h_s} + \frac{3h_a(h_a+h_s)^2}{E_a h_a^3+E_s h_s^3}$ is linearly increasing at low α and becomes constant at high α as shown in the inset. This means that the actuation stress-strain

relation of C-O-H in a bilayered actuator (Fig. 2f) is linear for the same α, but on increasing α the slope decreases towards a saturated value.

As the chemical characteristics described by Eq. (1) applies to the actuation stress σ_a at the topmost surface region where light is illuminated, the trend of σ_a against α will be analyzed next, as per Eq. (5). From Fig. 2g, σ_a is compressive throughout the whole range of α studied, with a significant increasing trend with α because of the $E_a h_a \kappa/2$ term in Eq. (5) that represents a higher compression at the top surface will be resulted from a higher h_a or α. From the inset, the term $D_a = \frac{E_a h_a^3 + E_s h_s^3}{6h_a(h_a+h_s)} - \frac{E_a\, h_a}{2}$ from Eq. (5) is almost linearly related with α within the range studied. That is to say, σ_a is dominated by the stress generated from bending, rather than the light-induced contraction.

Fig. 2h shows the ε_a^{chem} vs σ_a/E_a plots, for the range $\alpha < 0.3$ in which the data show more steady trends as in Fig. 2g. The ε_a^{chem} vs σ_a/E_a relations are rather linear, thus obeying Eq. (9). The slopes of the plots under the three different light intensities have similar values, so the mean value, 5.9, is taken as the estimated normalized activation volume ω of C-O-H according to Eq. (9). The activation volume Ω is calcaulated by multiplying $3kT/E_a$ to ω, giving the value of 4.3 Å^3. The y-intercepts of the plots in Fig. 2h give the normalized thermodynamic driving force ϕ according to Eq. (9), from which the driving force ΔE_{chem} is obtained as 2.1, 3.9 and 6.8×10^{-23} J respectively for the light intensities of 10, 20 and 50 mW/cm^2. The results for ϕ, shown as the inset in Fig. 2h, indicate that higher light intensity gives larger thermodynamic driving force to produce the actuation. Noticeably, the correlation coefficient (R^2 value) for the linear-fitting at 50mW/cm^2 is significantly smaller than that under lower light intensities, since at higher light intensity the actuation curvature is relatively larger and so minor differences in microstructure such as degree of crystallinity, impurities, and uniformity of thickness, become more influential.

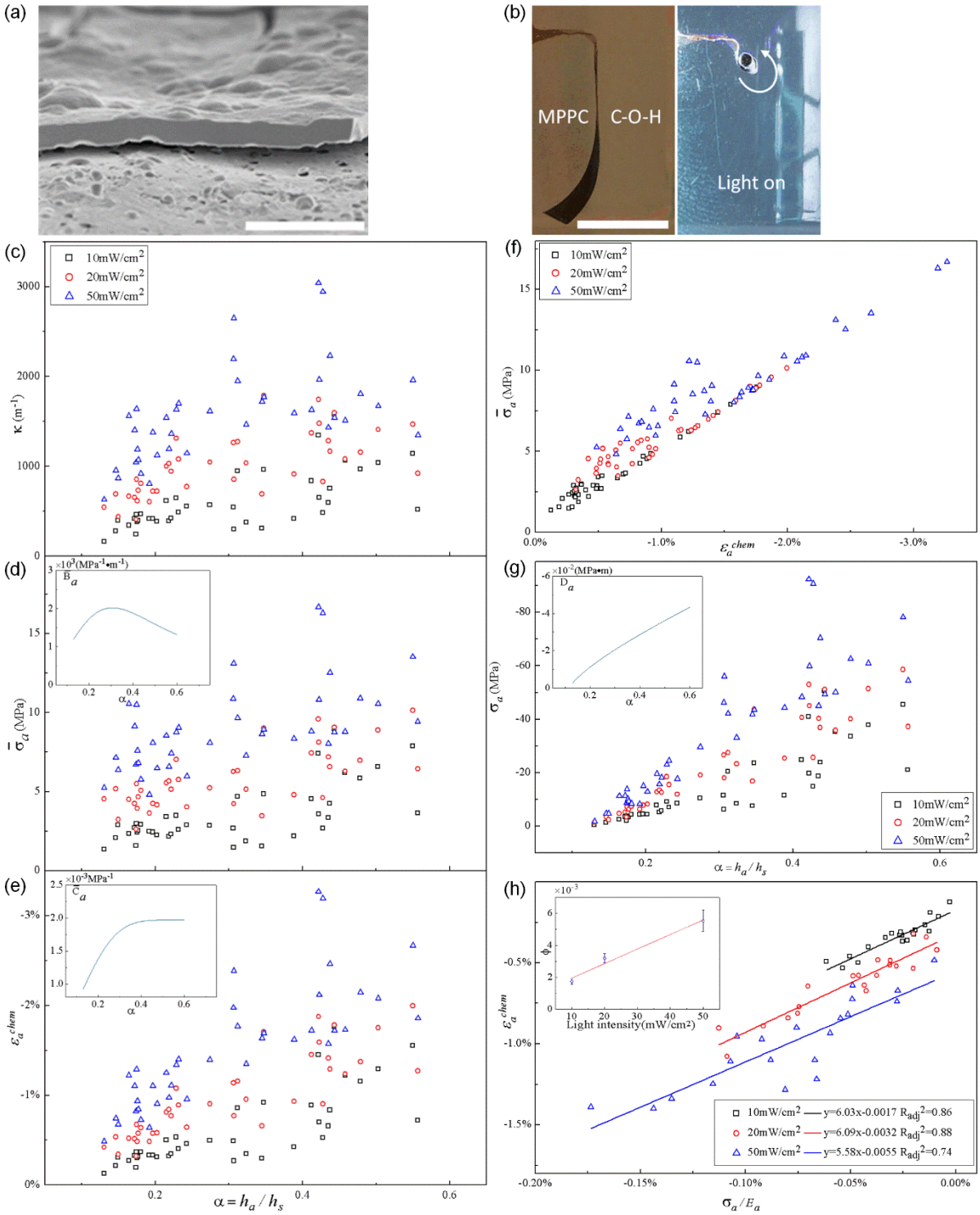

Fig. 2 Quantitative actuation performance of C-O-H/MPPC actuator with chemo-mechanical instability. (a) SEM micrograph of a typical C-O-H/MPPC bilayer actuator (scale bar: 10 μm). (b) Snapshots of a light actuation test induced by 50mW/cm^2 Vis light illumination (scale bar: 10 mm). (c) Curvature change (κ), (d) average actuation stress ($\bar{\sigma}_a$) with $\bar{B}_a$ (Eq. (2)) in the inset and (e) intrinsic actuation strain (ε_a^{chem}) with $\bar{C}_a$ in the inset plotted against α. (f) Average

actuation stress ($\bar{\sigma}_a$) plotted against intrinsic actuation strain (ε_a^{chem}). (g) σ_a plotted against α; inset shows term D_a (Eq. (5)) plotted against α. (h). $\varepsilon_a^{chem} - \frac{\sigma_a}{E_a}$ linear fitting from actuators of which α smaller than 0.3; inset shows the normalized driving force ϕ plotted against illuminating light intensity.

Similarly, the actuation performance of C-O-H actuators on Ni substrates (C-O-H/Ni) was investigated and shown in Fig. 3. Fig. 3a shows the bilayered structure with the C-O-H active layer on top of a Ni substrate. Fig. 3b shows that under 50mW/cm^2 Vis light illumination, the actuator bends towards the C-O-H side into multiple loops. In Fig. 3c, in contrary to the monotonically increasing trend for C-O-H/MPPC actuators shown in Fig. 2c, the curvature κ of C-O-H/Ni actuators peaks at approximately the same α value (≈ 2) under different illumination intensities, and after the hump, κ attains a constant value for a wide α range. Similar trends of κ versus α can be found for different light intensities, without significant fluctuations. $\bar{\sigma}_a$, however, undergoes a drop at small α, followed by steady rise, as shown in Fig. 3d. On the other hand, $\bar{B}_a = \frac{6h_a(h_a+h_s)}{E_a h_a^3 + E_s h_s^3}$, as shown in the inset of Fig. 3d, has a generally smaller value than that for C-O-H/MPPC within the range of α studied, leading to an overall higher $\bar{\sigma}_a$ for the C-O-H/Ni actuators. A higher, or more tensile, $\bar{\sigma}_a$ would be disadvantageus for actuation since a large compressive surface stress would not exist to enhance water de-intercalation in the surface region. In Fig. 3e, ε_a^{chem} is fairly constant when α is small and increases steadily with α when α is large. However, ε_a^{chem} for the C-O-H/Ni actuators has overall smaller values than the C-O-H/MPPC actuators. From the inset, $\bar{C}_a = \frac{1}{E_a} + \frac{h_a}{E_s h_s} + \frac{3h_a(h_a+h_s)^2}{E_a h_a^3 + E_s h_s^3}$ shows a similar trend as that for the C-O-H/MPPC actuators. Fig. 3f clearly shows that a higher light intensity gives higher magnitudes of $\bar{\sigma}_a$ and ε_a^{chem}, and linear relations hold between the two variables in the high α regime, due to the change of bending-dominated to stretching-dominated deformation, which is discussed in detail previously [28]. From Fig. 3g,

the surface stress σ_a is positive (tensile) at small α, and turns into negative (compressive) when α is large, while the numerical value of $D_a = \frac{E_a h_a^3 + E_s h_s^3}{6h_a(h_a+h_s)} - \frac{E_a\, h_a}{2}$, in a wider α range for the C-O-H/Ni actuators, increases drastically at small α and decreases mildly after reaching a peak, as shown in the inset. From Fig. 3h, although ε_a^{chem} and $\frac{\sigma_a}{E_a}$ exhibit relatively weaker linearity for the C-O-H/Ni actuators, the ω estimated from the slopes of best fitting lines has a much smaller value ($\omega \approx 0.5$) than that for the C-O-H/MPPC actuators, and a linear relation is found between the normalized thermodynamic driving force ϕ and the illuminating light intensity, as shown in the inset.

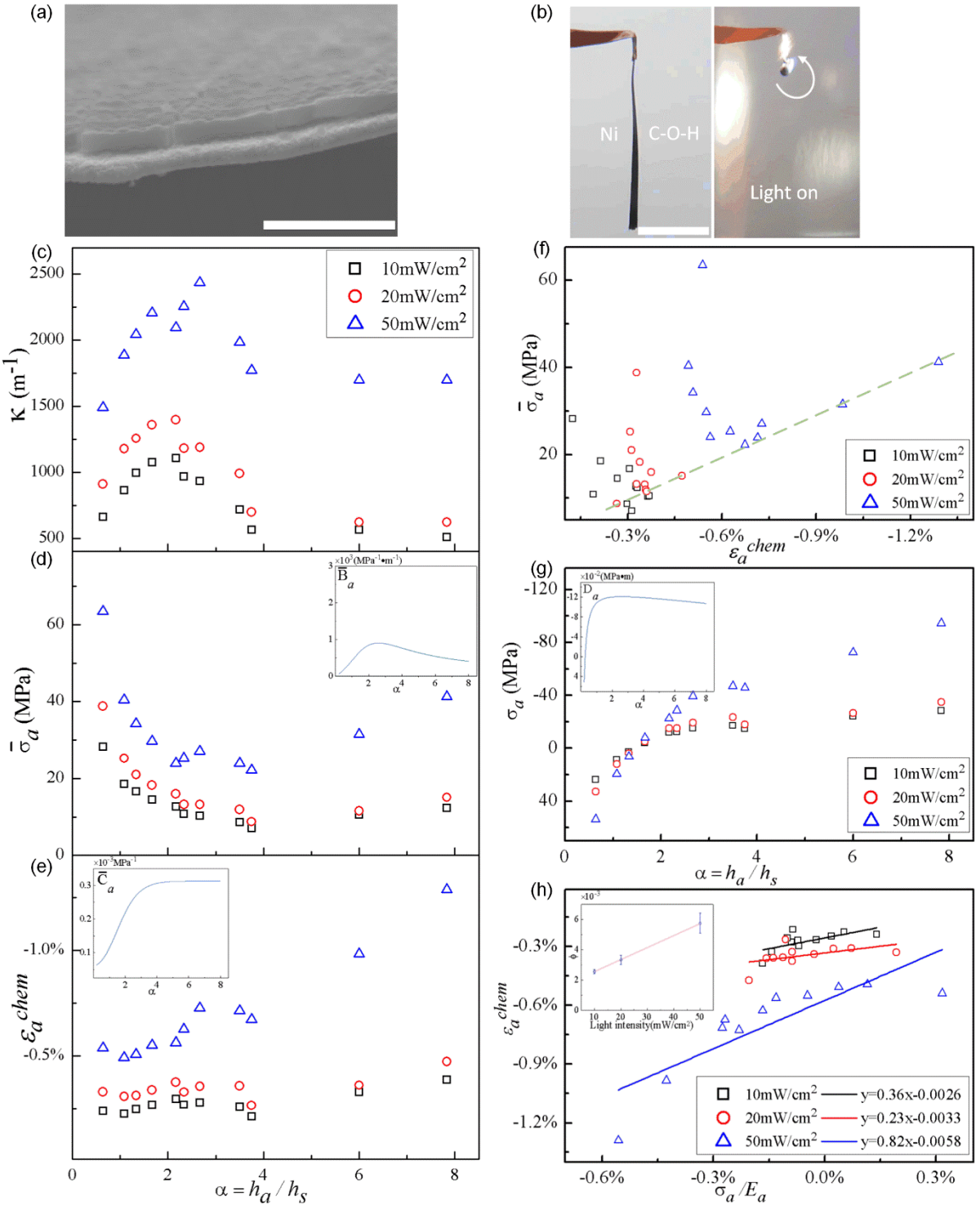

Fig. 3 Quantitative actuation performance of C-O-H/Ni actuators without chemo-mechanical instability. (a) SEM micrograph of a typical C-O-H/Ni bilayer actuator (scale bar: 10 μm). (b) Snapshots of a light actuation test induced by 50mW/cm^2 Vis light illumination (scale bar: 10 mm). (c) Curvature change (κ), (d) average actuation stress ($\bar{\sigma}_a$) with $\bar{B}_a$ (Eq. (2)) in the inset and (e) intrinsic actuation strain (ε_a^{chem}) with $\bar{C}_a$ in the inset plotted against α. (f) Average actuation stress ($\bar{\sigma}_a$) plotted against intrinsic actuation strain (ε_a^{chem}). (g) σ_a plotted against α; inset shows term D_a (Eq. (5)) plotted against α. (h) $\varepsilon_a^{chem} - \frac{\sigma_a}{E_a}$ linear fitting under different

light intensities; inset shows the normalized driving force ϕ plotted against illuminating light intensity.

3.2 Chemo-mechanical instability of C-O-H/MPPC and N-H-O/MPPC actuators

Fig. 1f shows the theoretical plot of the nomalized curvature $K(\alpha, \beta)$ according to Eq. (8), for the specific case of ω = 5.9 as determined from the slope of Eq. (9) using the data in Fig. 2h for the C-O-H/MPPC actuators. Since the ω value of 5.9 here exceeds the threshold of 2, the chemo-mechanical instability is expected to occur, and Fig. 1f indeed shows that K surges to infinity for certain values of α and β. For C-O-H deposited on MPPC, $\beta = E_a/E_s$ = 24.29 (E_a = 17 GPa for C-O-H, and E_s = 0.7 GPa for MPPC), and the theoretical plot of K vs α at this specific value of β is shown as the orange dotted curve in Fig. 4, where a singularity at $\alpha \sim 0.4$ can be seen. Note that according to the right side of Eq. (8), the normalized curvature K does not depend on the driving force ϕ, and, as Fig. 2h shows, the activation volume ω is roughly constant for the different light intensities studied; therefore the orange theoretical curve in Fig. 4 should apply to different light intensities. In Fig. 4, the discrete symbols are the experimental data of K as calculated from its definition $\kappa h_s/(\phi\beta^{1/3})$, using the experimentally measured κ data and ϕ values of 1.7, 3.2 and 5.5×10^{-3} for 10, 20, and 50 mW/cm^2, respectively, as determined from Fig. 2h according to Eq. (9). When $\alpha < 0.3$ where the fluctuations in K are smaller than 0.5 in magnitude, the experimental points under all three light intensities correlate well with the theoretical curve, but for α > 0.3, the actuation enters an unstable region, where the theoretical curve shows a surge followed by a sharp drop while the experimental data show significant fluctuations of around 1.5 in magnitude when illuminated by 20 and 50 mW/cm^2 Vis light, and more than 2.5 under 10 mW/cm^2 light. Considering the uncertainties in the measured α values, in the narrow range of α in which the chemo-mechanical instability occurs, a small change in α should lead to a large change in actuation, which explains the large

fluctuations in this range. Similar to the C-O-H/MPPC actuators, the N-H-O/MPPC system also has a large ω value of 7.6, and the corresponding theoretical curve (pink dotted) in Fig. 4 surges and plummets within a narrow α range due to the chemo-mechanical instability. Experimental data also show a sharp peak in this range.

On the contrary, C-O-H and N-H-O actuators fabricated on Ni substrates have ω values significantly smaller than the critical value of 2, and hence do not exhibit the chemo-mechanical instability. C-O-H/Ni actuators were fabricated and characterized as shown in Fig. 3, and as mentioned above (cf. Fig. 3h), ω falls in the range of 0.23-0.82 for the different light intensities studied. Previous data on N-H-O electrodeposited on Ni substrates (N-H-O/Ni) [5] were also analyzed, and the ω is found to be 0.6. Fig. 1e shows the theoretical plot of $K(\alpha, \beta)$ at $\omega = 0.55$ which is close to the values for both the C-O-H/Ni and N-H-O/Ni systems, where no singularity or instability exists. The β values for the C-O-H/Ni and N-H-O/Ni systems are rather similar at 0.077 and 0.11 respectively (Young's moduli for C-O-H, N-H-O and Ni are 17 GPa, 24 GPa and 220 GPa, respectively), and since their ω values are also close in the range of 0.3 to 0.8, only one theoretical curve (dark blue) corresponding to $\omega = 0.55$ and $\beta = 0.093$ (the mean values for the two systems) is shown to represent both systems of C-O-H/Ni and N-H-O/Ni, in order to make Fig. 4 more readable. It can be seen that the theoretical curve fits the experimental data well for both systems over a wide range of α, indicating good predictability of the present model. Also, for both actuator systems on Ni substrates with ω significantly smaller (≈ 0.55) than the critical value of 2, no instability occurs as shown. All in all, Fig. 4 shows that the chemo-mechanical model correctly predicts the actuation of four systems of bilayered actuators comprising the C-O-H and N-H-O actuating materials on either Ni or MPPC substrates, and, in particular, the occurrence of the chemo-mechanical instability.

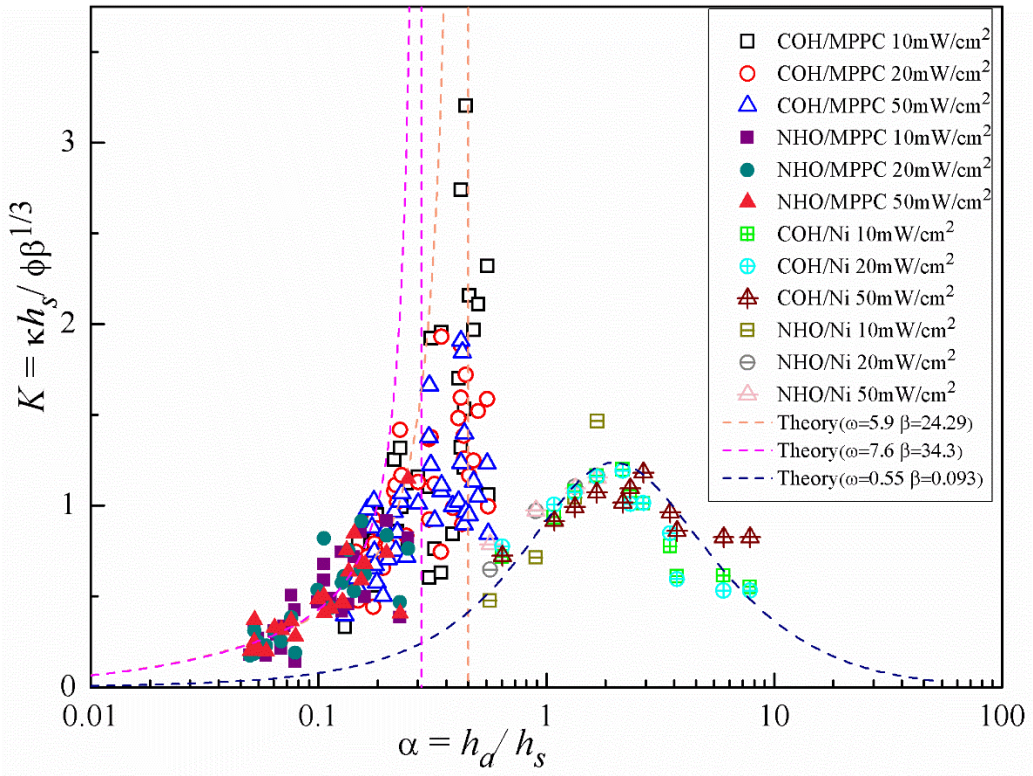

Fig. 4 Near-instability arises for C-O-H or N-H-O on MPPC substrates, where $\omega > 2$. For both actuation materials on Ni substrates, $\omega \approx 0.55$, and no instability occurs.

4. Discussion

The chemo-mechanical instability found in this study is a theoretical condition of unstable actuation for a bilayered actuator, when the stress-assisted chemical reaction that causes the actuation of the active material at the top, stimulated surface region receives a positive feedback from the compressive stress there as the actuator bends. According to Eq. (5), the surface stress can be significantly compressive as the actuator bends, even though the average stress $\bar{\sigma}_a$ is tensile to cause the bending. The compressive surface stress in turn enhances the water de-intercalation reaction according to Eq. (1), causing the near-surface region to contract and the actuator to bend more. This in turn generates an even higher surface compressive stress, which further enhances the water de-intercalation at the top surface region. Under such a positive feedback scenario, no equilibrium point can be reached between the chemical and mechanical characteristics of the system, and so the bending actuation of the bilayered cantilever would grow in an unstable fashion.

From our experiments, the instability occurs on MPPC substrates, with either C-O-H or N-H-O working as the active material, while this phenomenon is not observed from actuators with Ni substrates. To be more specific, the actuation performance of actuators supported by different substrates gives rise to different estimates of ω, with ω for actuators with MPPC substrates exceeding the instability threshold of 2 whereas that for actuators with Ni substrates not. However, why the normalized activation volume ω of the active layer varies significantly between MPPC and Ni substrates is an interesting question. Here, we postulate two potential reasons:

(1) The exact mechanism of how light triggers water de-intercalation from the turbostratic structure is still not well known, but there may well be a heating effect of the light that enhances the water de-intercalation. Our earlier work[5,28] shows that pure heating of the active material without light illumination can also cause it to contract, in a similar way as what light illumination will do. MPPC is a much better thermal insulator than Ni, so MPPC substrates can potentially enhance more the thermal effect of light when it is illuminated onto the active material, than Ni substrates. From photothermal measurements as shown in Fig. 5, the temperature increase for C-O-H/MPPC actuators is indeed found to be higher than that for C-O-H/Ni actuators with the same h_a under both 20 and 50mW/cm^2 illumination. The activation volume is a measure of the amount of water de-intercalated from the turbostratic structure in the rate-determining step, so an enhanced thermal effect should correspond to a larger ω.

(2) The microstructure or turbostratic structure of the C-O-H and N-H-O active materials may be different on the two types of substrates, thus producing different light-triggered response in the water de-intercalation process.

On the other hand, although the chemo-mechanical instability would indicate theoretically an extremely large actuation, under realistic circumstances, the bending actuation

cannot grow indefinitely due to a number of reasons. First, as the bending curvature rises to a large extent, certain parts of the cantilever actuator will be blocked from the stimuli (e.g. light illumination) by other parts. Secondly, the actuation mechanism is water de-intercalation, but the intercalated water content in the active layer is limited, so that the maximum actuation curvature attainable will be limited by the hydrophilicity of the actuating material. Thirdly, as the actuator bends into a large curvature, the large bending stress inside the active layer and at the bilayer interface may result in crack formation and growth or layer delamination. All these factors would limit the actuator performance even though the instability is prone to occur. The implication here can be both ways. First, to maintain the long-term structural integrity of the actuator, the instability should perhaps be avoided. However, if the material components and their interface are strong enough to withstand failure, actuators with tremendous actuation performance can be designed to operate in the instability regime. To be more specific, the active material can be engineered into a composite with hydrophilic components to enhance the hydrophilicity, and the active material can be mixed with a strengthening/toughening phase to reduce the possibility of stress-induced fracture. Then, the present chemo-mechanics model can be utilized to design actuators to operate in the instability regime with $\omega > 2$.

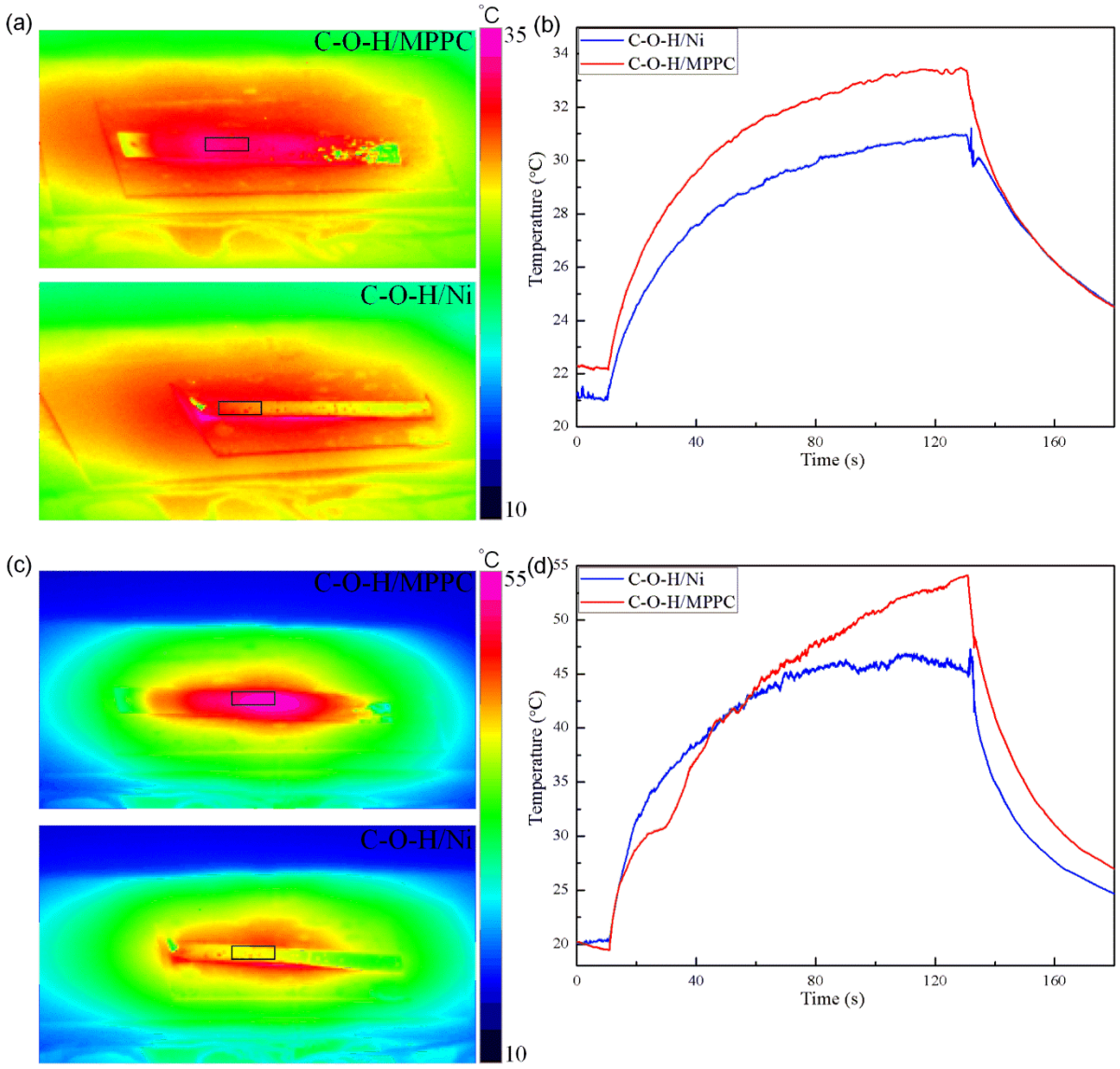

Fig. 5 Photothermal measurement of C-O-H/Ni and C-O-H/MPPC actuators ($h_a = 2.4 \pm 0.3$ μm for both cases) under 20 and 50 mW/cm^2 illumination. (a) Temperature maps after 2 mins at 20 mW/cm^2 illumination. (b) Temperature-time curves under 20 mW/cm^2 illumination. (c) Temperature maps after 2 mins at 50 mW/cm^2 illumination. (d) Temperature-time curves under 50 mW/cm^2 illumination.

5. Conclusion

A chemo-mechanics model is shown to be quantitively accurate for describing the actuation behavior of bilayered cantilever actuators comprising a stimuli-responsive layer that receives stimuli on its top surface and supported by a passive substrate layer. Based on this model, a novel chemo-mechanical instability is observed which results in extraordinarily large bending

actuation of the bilayer actuator. Experimental results on various active material-substrate couples show excellent agreement with the model and verify the existence of the chemo-mechanical instability under specific conditions as predicted.

Appendix

Writing E_aC_a in Eq. (11) as $E_aC_a = P/Q$, where $P = 3\alpha\beta(1+\alpha)^2 + (1+\alpha\beta)(1+\alpha^3\beta)$; $Q = 1 - \alpha^2\beta(2\alpha+3)$, it can be shown that if a local extremum for E_aC_a exists, then,

$$\frac{\partial P}{\partial \alpha}\frac{\partial Q}{\partial \beta} = \frac{\partial P}{\partial \beta}\frac{\partial Q}{\partial \alpha}$$

However, this would lead to $4\alpha + \alpha^3\beta + 3 = 0$, for which no solution would exist in the domain $\alpha, \beta > 0$. Therefore, in the domain $\alpha, \beta > 0$, the $E_aC_a(\alpha, \beta)$ surface exhibits no local extremum. Apart from the singularity along the $\beta = 1/\alpha^2(2\alpha+3)$ line, the extreme values for E_aC_a occurs at the boundaries of the domain $\alpha, \beta > 0$. For the inner branch $\beta < 1/\alpha^2(2\alpha+3)$, $E_aC_a(\alpha \to 0 \text{ or } \beta \to 0) \to 1$, so this branch is bounded below by 1. For the outer branch $\beta > 1/\alpha^2(2\alpha+3)$, $E_aC_a\left(\alpha \to \infty\right) \to -2$, and $E_aC_a\left(\beta \to \infty\right) \to -\infty$, so this branch is bounded above by -2. Therefore, the $E_aC_a(\alpha, \beta)$ function exhibits no value between -2 and 1 in the domain $\alpha, \beta > 0$.

Supplementary Information

Supplementary Video S1: Demo showing the visible light actuation of C-O-H/MPPC actuator.

Acknowledgments: This work was supported by Kingboard Endowed Professorship in Materials Engineering. The authors are grateful to Prof. Q.P. Sun and Mr. G. Zhou of the Hong Kong University of Science and Technology for their assistance in the photothermal measurements.

Author contributions:

Wenrui Ma: Investigation: performing experiments, data collection and calculation, Writing: original draft. **Kin Wa Kwan**: Investigation: performing experiments and calculation, Writing: original draft. **Runni Wu**: Investigation: performing experiments. **Alfonso H.W. Ngan**: Conceptualization, Methodology: creation of model, Investigation: calculation, Supervision, Writing - Review & Editing.

References

[1] F. Cheng, R. Yin, Y. Zhang, C.C. Yen, Y. Yu, Fully plastic microrobots which manipulate objects using only visible light, Soft Matter. 6 (2010) 3447–3449. https://doi.org/10.1039/c0sm00012d.

[2] S. Miyashita, S. Guitron, M. Ludersdorfer, C.R. Sung, D. Rus, An untethered miniature origami robot that self-folds, walks, swims, and degrades, Proc. - IEEE Int. Conf. Robot. Autom. 2015-June (2015) 1490–1496. https://doi.org/10.1109/ICRA.2015.7139386.

[3] M. Ji, N. Jiang, J. Chang, J. Sun, Near-infrared light-driven, highly efficient bilayer actuators based on polydopamine-modified reduced graphene oxide, Adv. Funct. Mater. 24 (2014) 5412–5419. https://doi.org/10.1002/adfm.201401011.

[4] B. Shin, J. Ha, M. Lee, K. Park, G.H. Park, T.H. Choi, K.J. Cho, H.Y. Kim, Hygrobot: A self-locomotive ratcheted actuator powered by environmental humidity, Sci. Robot. 3 (2018) 1–9. https://doi.org/10.1126/scirobotics.aar2629.

[5] K.W. Kwan, S.J. Li, N.Y. Hau, W. Di Li, S.P. Feng, A.H.W. Ngan, Light-stimulated actuators based on nickel hydroxide-oxyhydroxide, Sci. Robot. 3 (2018). https://doi.org/10.1126/scirobotics.aat4051.

[6] L. Liu, L. Su, Y. Lu, Q. Zhang, L. Zhang, S. Lei, S. Shi, M.D. Levi, X. Yan, The Origin of Electrochemical Actuation of MnO 2 /Ni Bilayer Film Derived by Redox

Pseudocapacitive Process, Adv. Funct. Mater. 29 (2019) 1–12. https://doi.org/10.1002/adfm.201806778.

[7] K.W. Kwan, N.Y. Hau, S.P. Feng, A.H.W. Ngan, Electrochemical actuation of nickel hydroxide/oxyhydroxide at sub-volt voltages, Sensors Actuators, B Chem. 248 (2017) 657–664. https://doi.org/10.1016/j.snb.2017.04.009.

[8] K. Kaneto, M. Kaneko, Y. Min, A.G. MacDiarmid, "Artificial muscle": Electromechanical actuators using polyaniline films, Synth. Met. 71 (1995) 2211–2212. https://doi.org/10.1016/0379-6779(94)03226-V.

[9] S.H. Aboutalebi, R. Jalili, D. Esrafilzadeh, M. Salari, Z. Gholamvand, S. Aminorroaya Yamini, K. Konstantinov, R.L. Shepherd, J. Chen, S.E. Moulton, P.C. Innis, A.I. Minett, J.M. Razal, G.G. Wallace, High-performance multifunctional Graphene yarns: Toward wearable all-carbon energy storage textiles, ACS Nano. 8 (2014) 2456–2466. https://doi.org/10.1021/nn406026z.

[10] Q.M. Wang, Q. Zhang, B. Xu, R. Liu, L.E. Cross, Nonlinear piezoelectric behavior of ceramic bending mode actuators under strong electric fields, J. Appl. Phys. 86 (1999) 3352–3360. https://doi.org/10.1063/1.371213.

[11] R. Pelrine, R. Kornbluh, J. Joseph, R. Heydt, Q. Pei, S. Chiba, High-field deformation of elastomeric dielectrics for actuators, Mater. Sci. Eng. C. 11 (2000) 89–100. https://doi.org/10.1016/S0928-4931(00)00128-4.

[12] M. Fuchiwaki, J.G. Martinez, T.F. Otero, Asymmetric Bilayer Muscles. Cooperative and Antagonist Actuation, Electrochim. Acta. 195 (2016) 9–18. https://doi.org/10.1016/j.electacta.2016.02.104.

[13] M. Amjadi, M. Sitti, High-Performance Multiresponsive Paper Actuators, ACS Nano. 10 (2016) 10202–10210. https://doi.org/10.1021/acsnano.6b05545.

[14] Q. Li, C. Liu, Y.H. Lin, L. Liu, K. Jiang, S. Fan, Large-strain, multiform movements

from designable electrothermal actuators based on large highly anisotropic carbon nanotube sheets, ACS Nano. 9 (2015) 409–418. https://doi.org/10.1021/nn505535k.

[15] Y. Hu, T. Lan, G. Wu, Z. Zhu, W. Chen, A spongy graphene based bimorph actuator with ultra-large displacement towards biomimetic application, Nanoscale. 6 (2014) 12703–12709. https://doi.org/10.1039/c4nr02768j.

[16] L. Chen, M. Weng, Z. Zhou, Y. Zhou, L. Zhang, J. Li, Z. Huang, W. Zhang, C. Liu, S. Fan, Large-Deformation Curling Actuators Based on Carbon Nanotube Composite: Advanced-Structure Design and Biomimetic Application, ACS Nano. 9 (2015) 12189–12196. https://doi.org/10.1021/acsnano.5b05413.

[17] H. Arazoe, D. Miyajima, K. Akaike, F. Araoka, E. Sato, T. Hikima, M. Kawamoto, T. Aida, An autonomous actuator driven by fluctuations in ambient humidity, Nat. Mater. 15 (2016) 1084–1089. https://doi.org/10.1038/nmat4693.

[18] Y. Tai, G. Lubineau, Z. Yang, Light-Activated Rapid-Response Polyvinylidene-Fluoride-Based Flexible Films, Adv. Mater. 28 (2016) 4665–4670. https://doi.org/10.1002/adma.201600211.

[19] Y. Hu, G. Wu, T. Lan, J. Zhao, Y. Liu, W. Chen, A Graphene-Based Bimorph Structure for Design of High Performance Photoactuators, Adv. Mater. 27 (2015) 7867–7873. https://doi.org/10.1002/adma.201502777.

[20] M. Dai, O.T. Picot, J.M.N. Verjans, L.T. De Haan, A.P.H.J. Schenning, T. Peijs, C.W.M. Bastiaansen, Humidity-responsive bilayer actuators based on a liquid-crystalline polymer network, ACS Appl. Mater. Interfaces. 5 (2013) 4945–4950. https://doi.org/10.1021/am400681z.

[21] S. Taccola, F. Greco, E. Sinibaldi, A. Mondini, B. Mazzolai, V. Mattoli, Toward a new generation of electrically controllable hygromorphic soft actuators, Adv. Mater. 27 (2015) 1668–1675. https://doi.org/10.1002/adma.201404772.

[22] Y. Cheng, K. Ren, D. Yang, J. Wei, Bilayer-type fluorescence hydrogels with intelligent response serve as temperature/pH driven soft actuators, Sensors Actuators, B Chem. 255 (2018) 3117–3126. https://doi.org/10.1016/j.snb.2017.09.137.

[23] X.W. Dong, B. Wang, K.F. Wang, J.G. Wan, J.M. Liu, Ultra-sensitive detection of magnetic field and its direction using bilayer PVDF/Metglas laminate, Sensors Actuators, A Phys. 153 (2009) 64–68. https://doi.org/10.1016/j.sna.2009.04.033.

[24] E. Reyssat, L. Mahadevan, Hygromorphs: From pine cones to biomimetic bilayers, J. R. Soc. Interface. 6 (2009) 951–957. https://doi.org/10.1098/rsif.2009.0184.

[25] C.H. Hsueh, Modeling of elastic deformation of multilayers due to residual stresses and external bending, J. Appl. Phys. 91 (2002) 9652–9656. https://doi.org/10.1063/1.1478137.

[26] C. Cheng, A.H.W. Ngan, Reversible electrochemical actuation of metallic nanohoneycombs induced by pseudocapacitive redox processes, ACS Nano. 9 (2015) 3984–3995. https://doi.org/10.1021/nn507466n.

[27] S. Timoshenko, Analysis of Bi-Metal Thermostats, J. Opt. Soc. Am. 11 (1925) 233. https://doi.org/10.1364/JOSA.11.000233.

[28] K.W. Kwan, A.H.W. Ngan, A High-Performing, Visible-Light-Driven Actuating Material Responsive to Ultralow Light Intensities, Adv. Mater. Technol. 4 (2019) 1–8. https://doi.org/10.1002/admt.201900746.

[29] B. V. Robinson, F.M. Sullivan, J.F. Borzelleca, S.L. Schwartz, PVP, Routledge, 2018. https://doi.org/10.1201/9780203741672.

[30] L.S. Taylor, F.W. Langkilde, G. Zografi, Fourier transform Raman spectroscopic study of the interaction of water vapor with amorphous polymers, J. Pharm. Sci. 90 (2001) 888–901. https://doi.org/10.1002/jps.1041.